10.1098/rspa.2003.1270

THE ROYAL SOCIETY

Dynamics of poroelastic filaments

By J. M. Skotheim and L. Mahadevan†

Department of Applied Mathematics and Theoretical Physics, University of Cambridge, Wilberforce Road, Cambridge CB3 0WA, UK
(lm@deas.harvard.edu)

Received 26 May 2003; accepted 14 November 2003; published online 20 April 2004

We investigate the stability and geometrically nonlinear dynamics of slender rods made of a linear isotropic poroelastic material. Dimensional reduction leads to the evolution equation for the shape of the *poroelastica* where, in addition to the usual terms for the bending of an elastic rod, we find a term that arises from fluid–solid interaction. Using the *poroelastica* equation as a starting point, we consider the load-controlled and displacement-controlled planar buckling of a slender rod, as well as the closely related instabilities of a rod subjected to twisting moments and compression when embedded in an elastic medium. This work has applications to the active and passive mechanics of thin filaments and sheets made from gels, plant organs such as stems, roots and leaves, sponges, cartilage layers and bones.

Keywords: poroelasticity; buckling instability; rods; filaments; sheets; gels

1. Introduction

Poroelasticity is the continuum theory used to describe the behaviour of a biphasic material in which fluid flow is coupled to the elastic deformation of a solid skeleton (see Selvadurai (1996), Wang (2000) and references therein). The first applications of this theory were to geological problems such as consolidation of saturated soil under a uniform load (Biot 1941). Since then the theory has grown to cover many and varied applications, some of which are displayed in table 1.

If a medium having interstitial fluid of viscosity ν is forced to oscillate with a characteristic time τ, the Stokes length of the motion, $L_\mathrm{s} = \sqrt{\nu\tau}$, will characterize the range of influence of the solid into the fluid. If $L_\mathrm{s} \ll l_\mathrm{p}$ (the pore length-scale), the fluid within the pores moves out of phase relative to the solid. On the other hand, if $L_\mathrm{s} \gg l_\mathrm{p}$, the fluid will only move relative to the solid when the volume fraction of the solid matrix changes locally. This limit ($L_\mathrm{s} \gg l_\mathrm{p}$) was first considered by Biot (1941) for an isotropic poroelastic material. Later work using averaging techniques led to equations of the same form as well an understanding of how the microstructure of the material influences the constitutive equations of the material (Auriault & Sanchez-Palencia 1977; Burridge & Keller 1981; Mei & Auriault 1989; Lydzba & Shao 2000).

Whereas geological applications are concerned primarily with bulk behaviour, many engineering, physical and biological applications have extreme geometries

† Present address: Division of Engineering and Applied Sciences, Harvard University, Cambridge, MA 02138, USA.

which allow for the application of asymptotic methods to reduce the dimension of the problem. Some examples include the active and passive mechanics of thin filaments and sheets made of gels, plant organs such as stems, roots and leaves, sponges, cartilage layers, bones, etc.

In this paper we use the constitutive behaviour of a linear isotropic poroelastic solid to investigate the stability and dynamics of slender rods made of this material. In § 2 we give a physically motivated derivation of the constitutive equations for a poroelastic material. In § 3 we use the bulk poroelastic constitutive equations to determine the equation for the time-dependent bending of a slender poroelastic rod subjected to an externally applied compressive force P. Dimensional reduction leads to the equation for the *poroelastica*, where in addition to the usual terms due to the bending of an elastic rod we find a term due to the fluid resistance. It arises from the fluid–solid interaction and has a form similar to that in a Maxwell fluid (Bird *et al*. 1987). In § 4 we solve the problem of load-controlled buckling. Although the poroelastic nature of the material does not change the buckling threshold or the final stable shape, it governs the dynamics of the system as it evolves from the unstable to the stable state. Both the short and the long-time limit are investigated using asymptotic methods. We then use numerical methods to corroborate our asymptotic approaches and follow the nonlinear evolution of the poroelastica. In § 5 we treat the problem of displacement-controlled buckling and compare the results of the *poroelastica* with those of the classical *elastica* under similar loading conditions. In § 6 we consider the linear instability of a slender poroelastic filament embedded in an infinite elastic medium, when it is subjected to an axial twisting moment and an axial thrust. Finally, in § 7, we summarize our results and discuss possible applications to such problems as the mechanics of cartilaginous joints and rapid movements in plants.

2. Governing equations for poroelastic media

We begin with the equations for a homogeneous, elastic isotropic poroelastic material in the limit where the Stokes length, $L_\mathrm{s} = \sqrt{\nu\tau}$ is much larger than the system size l_m and further that l_m is much larger than the pore size l_p. We will also neglect inertial effects in the solid and liquid phases. In this limit the viscous resistance to fluid flow in the pores is balanced by the pressure gradient, so that the momentum balance in the fluid yields

$$\rho\nu\nabla^2_{l_\mathrm{p}}\boldsymbol{v} - \nabla p - \nabla_{l_\mathrm{p}} p_\mathrm{p} = 0, \tag{2.1}$$

where $\boldsymbol{v}$ is the fluid velocity with characteristic scale V, ρ is the fluid density, ∇ and ∇_{l_p} denote gradients on the system scale and the pore scale, respectively, p is the macroscopic pressure driving the flow, and p_p is the microscopic pressure in the pore. When the pore scale and system size are well separated ($l_\mathrm{p}/l_\mathrm{m} \ll 1$), equation (2.1) gives the following scaling relations:

$$p \sim \frac{l_\mathrm{m}\rho\nu V}{l_\mathrm{p}^2} \gg \frac{\rho\nu V}{l_\mathrm{p}} \sim p_\mathrm{p}. \tag{2.2}$$

Thus, the dominant contribution to the fluid stress in the medium arises from the macroscopic pressure. The simplest stress–strain law for the composite medium then arises by considering the linear superposition of the dominant components of the fluid

and solid stress tensor. Assuming that the elastic behaviour of the solid skeleton is characterized well by Hookean elasticity (i.e. the strains are small), we can write the following constitutive equation for the poroelastic medium (see Appendix A for a derivation using the method of multiple scales):

$$\boldsymbol{\sigma} = 2\mu\boldsymbol{e} + \lambda\nabla\cdot\boldsymbol{u}\boldsymbol{I} - \alpha p\boldsymbol{I}. \tag{2.3}$$

Here $\boldsymbol{\sigma}$ is the stress tensor, $\boldsymbol{u}$ is the displacement field, $\boldsymbol{e} = \frac{1}{2}(\nabla\boldsymbol{u} + \nabla\boldsymbol{u}^{\mathrm{T}})$ is the linearized strain, μ and λ are the effective Lamé coefficients of the material (dependent on the material properties *and* the microstructure), α is related to the fluid volume fraction but includes a contribution from the dilatation of the solid skeleton as it is compressed by the pressure in the surrounding fluid (see Appendix A), and $\boldsymbol{I}$ is the identity tensor in three dimensions. These material parameters can be derived using microstructural information (see Appendix A). In the limit when inertia can be neglected, the equations of equilibrium are

$$\nabla\cdot\boldsymbol{\sigma} = 0. \tag{2.4}$$

Mass conservation and continuity requires that the rate of dilatation of the solid is balanced by the differential motion between the solid and fluid in a poroelastic solid. This yields (see Appendix A for a derivation using the method of multiple scales)

$$\nabla\cdot\boldsymbol{k}\cdot\nabla p = \beta\partial_t p + \alpha\partial_t\nabla\cdot\boldsymbol{u}, \tag{2.5}$$

where the solid skeleton is composed of a material with bulk modulus β^{-1} ($\neq \lambda + \frac{2}{3}\mu$, since the Lamé coefficients λ and μ are for the composite material and take into account the microstructure, while β^{-1} is independent of the microstructure) and $\boldsymbol{k}$ is the fluid permeability tensor of the solid matrix. In words, (2.5) states that the flux of fluid into a material element is balanced by the change in solid volume due to the bulk compressibility of the matrix. For a rigid incompressible skeleton, $\beta = 0$. We will assume that the solid skeleton is isotropic so that $\boldsymbol{k} = k\boldsymbol{I}$; however, many structured and biological materials are anisotropic, and one may need to revisit this assumption. Equations (2.3)–(2.5), when subjected to appropriate boundary conditions, describe the evolution of displacements $\boldsymbol{u}$ and fluid pressure p in a poroelastic medium. The typical values of the parameters for a soft gel are $\alpha \sim 1$, $\mu \sim \lambda \sim 10^6$ Pa, and $k \sim 10^{-12}\ \mathrm{m}^2\ \mathrm{s}^{-1}\ \mathrm{Pa}^{-1}$.

3. Equations of motion for a slender filament

We consider a naturally straight slender circular rod of length L and radius $R \ll L$ with a tangent to the centreline that makes an angle θ with the horizontal (see figure 1). At its ends an axial force P is applied suddenly at time $t = 0$. We will further assume that the lateral surfaces of the filament are free of tractions. This assumption could break down when the solid matrix is very dilute, so that interfacial forces become comparable with the internal forces in the filament, but we will not consider this case here. The slenderness of the filament implies that the axial stresses vary rapidly across the cross-section and much more slowly along it, so that we can use an averaging procedure to deduce low-dimensional equations that describe the motion of the filament. This long-wavelength approximation can be formalized using an asymptotic expansion in the aspect ratio of the filament $R/L \ll 1$. Here, we will

Table 1. *Applications of poroelasticity*

($L_s = \sqrt{\nu\tau}$ is the Stokes length, where ν is the kinematic viscosity of the interstitial liquid and τ is the time-scale of the motion.)

	geometry	
	infinite medium	finite medium
$L_s \sim$ pore size	high-frequency acoustic wave propagation in saturated rock	sound absorption
		high-frequency vibrating gels/ biological tissues
$L_s \gg$ pore size	low-frequency acoustic wave propagation in saturated rock	low-frequency vibrating gels/ biological tissues
	consolidation and settling phenomena	bone mechanics
		cartilage deformation
		dynamics of poroelastic filaments

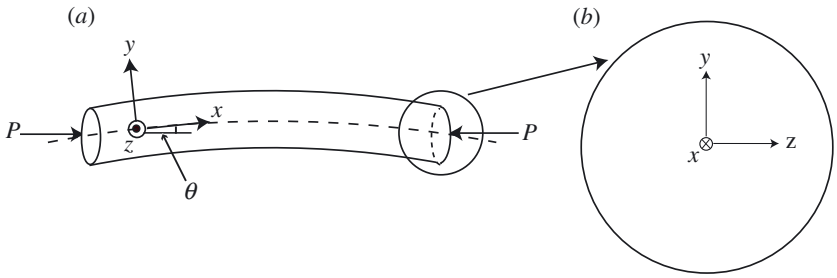

Figure 1. Schematic of (a) a bent rod, where $\theta(x)$ is the angle between the deformed and undeformed tangent vector and x, y and z are body-fixed coordinates in the reference frame of the rod; (b) the circular cross-section.

proceed directly by noting that, since the rod is slender, bending it is easier than stretching or shearing it (Love 1944). At the level of scaling, geometry implies that the out-of-line (bending) displacement of the centreline scales as R, while the axial displacement scales as R^2/L.

At the surface of the filament, no stress is applied. Since the filament is thin, this implies that $\sigma_{yy} \approx \sigma_{zz} \approx 0$. For a displacement field $\boldsymbol{u} = (u_x, u_y, u_z)$, equation (2.3) yields

$$\sigma_{yy} = -\alpha p + (2\mu + \lambda)\partial_y u_y + \lambda(\partial_x u_x + \partial_z u_z) = 0, \tag{3.1}$$

$$\sigma_{zz} = -\alpha p + (2\mu + \lambda)\partial_z u_z + \lambda(\partial_x u_x + \partial_y u_y) = 0, \tag{3.2}$$

which can be solved for $\partial_y u_y$ and $\partial_z u_z$ to give

$$\partial_y u_y = \partial_z u_z = \frac{\alpha p - \lambda \partial_x u_x}{2(\mu + \lambda)}. \tag{3.3}$$

Equations (2.3) and (3.3) give the axial stress

$$\sigma_{xx} = -\frac{\alpha\mu}{\lambda+\mu}p + \frac{3\lambda\mu+2\mu^2}{\lambda+\mu}\,\partial_x u_x. \tag{3.4}$$

More specifically, when an infinitesimal axial element of the rod of length $\mathrm{d}x$ is bent so that locally the centreline curvature is $\partial_x\theta$, fibres that are parallel to the neutral axis (coincident with the centreline for a homogeneous circular cross-section) and at a perpendicular distance y from the neutral plane (defined by the neutral axis and the axis of bending) will be either extended or contracted by an amount $y\partial_x\theta\,\mathrm{d}x$, so that the elastic strain $\partial_x u_x = -y\partial_x\theta$. This leads to an elastic stress that varies linearly across the cross-section; in addition, there is a fluid pressure that is determined by equation (2.5). We insert (3.3) into (2.5) and find the evolution equation for the fluid pressure:

$$k(\partial_{xx}p + \partial_{yy}p + \partial_{zz}p) = \left(\beta + \frac{\alpha^2}{\lambda+\mu}\right)\partial_t p - \frac{\alpha\mu}{\lambda+\mu}y\,\partial_{xt}\theta. \tag{3.5}$$

To make the equations dimensionless, we use the following definitions for the dimensionless primed variables:

$$\left.\begin{aligned} x = Lx', \qquad y = Ry', \qquad z = Rz', \qquad \theta = \frac{R}{L}\theta', \\ \sigma_{xx} = \frac{(2\mu^2+3\lambda\mu)R^2}{(\mu+\lambda)L^2}\sigma'_{xx}, \qquad P = \frac{\pi(2\mu^2+3\lambda\mu)R^4}{4(\mu+\lambda)L^2}P', \\ p = \frac{\alpha\mu R^2}{[(\mu+\lambda)\beta+\alpha^2]L^2}p', \qquad t = \frac{[(\mu+\lambda)\beta+\alpha^2]R^2}{(\mu+\lambda)k}t', \end{aligned}\right\} \tag{3.6}$$

and then immediately drop the primes, referring exclusively to dimensionless variables from now on. We note that the axial stress, the compressive force and the pressure are scaled to reflect the dominance of bending deformations over all other modes, and the time is scaled to reflect the dominance of radial diffusion over axial diffusion.

The stress in the filament, given by (3.4), can then be written in a dimensionless form as

$$\sigma_{xx} = -y\,\partial_x\theta - \tfrac{1}{4}\delta p. \tag{3.7}$$

Here, the first term reflects the purely elastic contribution well known from the theory of beams (Love 1944), while the second term is proportional to the fluid pressure in the pores. The dimensionless parameter

$$\delta = \frac{4\alpha^2\mu}{(2\mu+3\lambda)[(\mu+\lambda)\beta+\alpha^2]} \sim O(1)$$

for most materials denotes the ratio of the fluid and solid stress.

In the long-wavelength approximation, it is preferable to use the stress resultant

$$F = \int \sigma_{xx}\,\mathrm{d}A$$

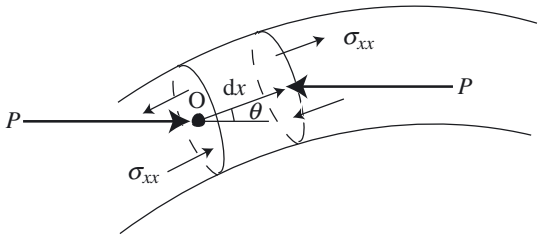

Figure 2. Schematic of the local torque balance in a bent rod under an externally applied compression P. We balance torques about the point O; x, y and z are the coordinates in the body-fixed frame with O as the origin. Let $M(x)$ denote the total moment due to internal stresses generated in part by bending the elastic skeleton and in part by the fluid pressure field. Balancing torques gives: $M(x+\mathrm{d}l)-M(x)+\mathrm{d}l\times P=0$. In the limit $\mathrm{d}l\to 0$, $\partial_x M+P\sin\theta=0$. The total moment $M=E_\mathrm{p}I\partial_x\theta+\alpha\int py\,\mathrm{d}A$, where E_p is the effective elastic modulus of the poroelastic skeleton and I is the moment of inertia of the cross-section.

and the torque resultant

$$M=-\int y\sigma_{xx}\,\mathrm{d}A=\int y^2\partial_x\theta\,\mathrm{d}A+\tfrac{1}{4}\delta\int yp\,\mathrm{d}A=M_\mathrm{e}+M_\mathrm{f}$$

as the variables of interest. Here M_e is the elastic torque and M_f is the fluid torque that arises due the transient effects of a pressure gradient across the filament. Then, the local force and torque balance, which can be derived from (2.3), (2.4) and (3.4), or equivalently directly (figure 2), yields the dimensionless equations

$$\left.\begin{aligned}\partial_x F&=0,\\ \partial_x M+\tfrac{1}{4}\pi P\sin\theta&=0.\end{aligned}\right\}\tag{3.8}$$

The first of these equations can be integrated immediately to yield $F=P$, with P a constant determined by the boundary conditions. The second equation combines the effects of the elastic and fluid stresses that arise due to the fluid pressure, and requires the solution of the continuity equation (3.5). For a rod with a circular cross-section, there is rotational symmetry in the problem. Choosing the axis of bending to coincide with the z-axis, we rewrite (3.5) in polar coordinates (r,ϕ), using dimensionless variables, as

$$\partial_t p-\frac{1}{r}\partial_r(r\partial_r p)-\frac{1}{r^2}\partial_{\phi\phi}p=r\sin\phi\partial_{xt}\theta.\tag{3.9}$$

We see that the pressure in the fluid arises from the extensional and compressional stresses in the filament due to bending. The boundary conditions for the pressure can be deduced using the following considerations: the centreline of the rod does not suffer any deformation, and is symmetrically disposed; the pressure at the surface is determined by the permeability of the surface layers and the flux through it. Then

$$\left.\begin{aligned}p&=0\quad\text{at } r=0,\\ Bip+\partial_r p&=0\quad\text{at } r=1,\end{aligned}\right\}\tag{3.10}$$

where $Bi=(\eta R)/k$, and η characterizes the flux through the surface for a given pressure drop (the ambient external pressure is assumed to be zero). The second

boundary condition in (3.10) on the pressure states that the flux of fluid through the surface is proportional to the pressure drop across the surface. $Bi = \infty$ corresponds to a freely draining rod, where there is no pressure jump across the surface, and $Bi = 0$ corresponds to a jacketed rod, which allows no flux through the surface. For a sponge, $Bi > 1$, while for a plant (root, stem or leaf) $Bi < 1$, since it is designed to retain water.

Expanding p in terms of the homogeneous solutions of (3.9), we write

$$p = \sum_{m=0}^{\infty} \sum_{n=1}^{\infty} [A_{mn} \sin m\phi + B_{mn} \cos m\phi] J_m(r\sqrt{\lambda_{mn}})\, \mathrm{e}^{-\lambda_{mn} t}, \tag{3.11}$$

where A_{mn} and B_{mn} are constants, J_m is the Bessel function of order m, and λ_{mn} is determined by the boundary conditions. Inspection of the inhomogeneous term on the right-hand side of equation (3.9) yields $m = 1$ so that $A_{1n} = A_n$, $B_{mn} = 0$ and $\lambda_{1n} = \lambda_n$. Since the boundary condition is a linear combination of p and $\partial_r p$, we are guaranteed to have a complete basis. We therefore look for a solution to the inhomogeneous equation (3.9) of the form

$$p = \sum_{n=1}^{\infty} A_n(t) \sin \phi J_1(r\sqrt{\lambda_n}), \tag{3.12}$$

where λ_n is determined by substituting (3.12) into (3.10), which yields

$$\partial_r J_1(r\sqrt{\lambda_n}) + Bi\, J_1(r\sqrt{\lambda_n}) = 0 \quad \text{at } r = 1. \tag{3.13}$$

Inserting (3.12) into (3.9) yields

$$\sum_{n=1}^{\infty} (\partial_t A_n + \lambda_n A_n) J_1(r\sqrt{\lambda_n}) = r\, \partial_{xt}\theta. \tag{3.14}$$

Multiplying (3.14) by $rJ_1(r\sqrt{\lambda_{n'}})$ and integrating across the cross-section gives

$$\partial_t A_n + \lambda_n A_n = \chi_n\, \partial_{xt}\theta, \tag{3.15}$$

where

$$\chi_n = \frac{\int_0^1 r^2 J_1(r\sqrt{\lambda_n})\, \mathrm{d}r}{\int_0^1 r[J_1(r\sqrt{\lambda_n})]^2\, \mathrm{d}r}. \tag{3.16}$$

Solving equation (3.15) yields

$$A_n = \chi_n \int_0^t \mathrm{e}^{-\lambda_n (t-t')} \partial_{xt'}\theta\, \mathrm{d}t', \tag{3.17}$$

so that (3.12) may be rewritten as

$$p = \sum_{n=1}^{\infty} \chi_n \sin \phi J_1(r\sqrt{\lambda_n}) \int_0^t \mathrm{e}^{-\lambda_n (t-t')} \partial_{xt'}\theta\, \mathrm{d}t'. \tag{3.18}$$

Then (3.7) allows us to write the total axial stress σ_{xx} at a cross-section as

$$\sigma_{xx} = -r \sin \phi \partial_x \theta - \tfrac{1}{4}\delta \sum_{n=1}^{\infty} \chi_n \sin \phi J_1(r\sqrt{\lambda_n}) \int_0^t \mathrm{e}^{-\lambda_n (t-t')} \partial_{xt'}\theta\, \mathrm{d}t'. \tag{3.19}$$

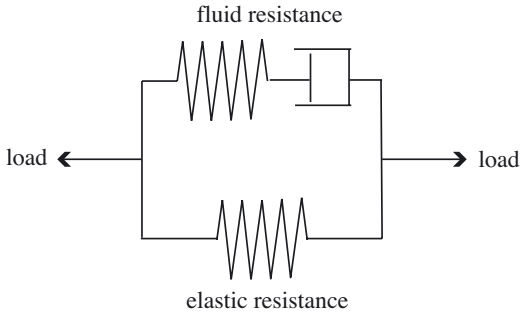

Figure 3. Mechanical analogue of the bending resistance of a poroelastic rod. For rapid displacements, the dashpot will not move and the fluid resistance due to the instantaneous pressure yields a response similar to a stiff (fluid) spring in parallel with an elastic spring. Eventually the dashpot will move to relieve the stress in the spring and the fluid resistance gradually decays, leading to a purely elastic steady state.

The dimensionless torque resultant is then given by

$$M = -\int r \sin\phi \sigma_{xx} \, \mathrm{d}A = \tfrac{1}{4}\pi\partial_x\theta + \tfrac{1}{4}\pi\delta \sum_{n=1}^{\infty} \gamma_n \int_0^t \mathrm{e}^{-\lambda_n(t-t')} \partial_{xt'}\theta \, \mathrm{d}t', \tag{3.20}$$

where

$$\gamma_n = \chi_n \int_0^1 r^2 J_1(r\sqrt{\lambda_n}) \, \mathrm{d}r.$$

Substituting the result into the equation for torque balance (3.8) yields the dimensionless equation for the poroelastica (see figure 2),

$$\partial_{xx}\theta + P\sin\theta + \delta \sum_{n}^{\infty} \gamma_n \int_0^t \mathrm{e}^{-\lambda_n(t-t')} \partial_{xxt'}\theta \, \mathrm{d}t' = 0. \tag{3.21}$$

The first two terms correspond to the usual terms in the classical elastica (Love 1944) for the bending of a rod with a circular cross-section, while the final term is due to the instantaneous fluid pressure not being equilibrated across the cross-section. The influence of the fluid is to create a material with 'memory', so that the current state of the filament is determined by its entire history. The kernel in the memory function for the fluid resistance is $\mathrm{e}^{-\lambda_n(t-t')}$, so that the fluid resistance is analogous to that of a Maxwell fluid (Bird *et al.* 1987) with relaxation times $1/\lambda_n$ which measure the rate of decay of the nth transverse mode in response to the rate of change of the curvature of the filament $\partial_{xt}\theta$. A mechanical analogue of the resistance of a poroelastic filament is presented in figure 3 and shows the connection to simple viscoelastic models.

The dynamics of a poroelastic rod are then determined by the solution of the equation for local torque balance (3.21), subject to the boundary condition on the fluid pressure at the surface (3.13), which determines the decay constants λ_n, and additional boundary conditions on the ends of the rod, which we now consider in some specific cases.

4. Planar load-controlled buckling

When an initially straight rod that is simply supported at either end is subjected to a constant compressive force P that is applied suddenly at $t = 0$, the boundary

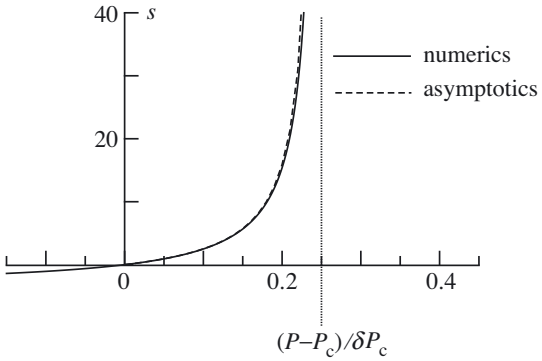

Figure 4. Growth rate s of the deflection as a function of the dimensionless external load P; $P_c = \pi^2$ is the critical compression above which a simply supported purely elastic rod buckles. Here the surface permeability parameter $Bi = 0.1$. When $(P - P_c)/\delta P_c = \frac{1}{4}$, the growth rate becomes infinite and one must consider inertial effects, which are neglected here. For comparison, we show the numerical results obtained by solving (3.21) with initial conditions $\theta(0) = 0.001 \cos \pi x$, $\theta(\mathrm{d}t) = 0.001 \mathrm{e}^{s\,\mathrm{d}t} \cos \pi x$, where s is the theoretically calculated exponent, with $\mathrm{d}t = 0.001$, $\mathrm{d}x = 0.01$.

conditions at the ends are

$$\left.\begin{aligned} \partial_x \theta(0,t) &= 0, \\ \partial_x \theta(1,t) &= 0, \end{aligned}\right\} \tag{4.1}$$

and the initial condition is

$$\theta(x,0) = 0. \tag{4.2}$$

The complete time evolution of the rod is then given by the solution of the integro-differential equation (3.21) subject to the boundary conditions (4.1), the initial conditions (4.2) and the condition (3.13) which determines the rate constants λ_n.

(*a*) *Short-time behaviour, $t \ll 1$*

Expanding the solution about the initially straight state $\theta = 0$, we write

$$\theta = \epsilon \theta_1(t), \tag{4.3}$$

where $\epsilon \ll 1$. Substituting the expression (4.3) into equation (3.21) and linearizing yields

$$\partial_{xx}\theta_1 + P\theta_1 + \delta \sum_{n=1}^{\infty} \gamma_n \int_0^t \mathrm{e}^{-\lambda_n (t-t')} \partial_{xxt'} \theta_1 \, \mathrm{d}t' = 0, \tag{4.4}$$

subject to the boundary conditions

$$\partial_x \theta_1(0,t) = \partial_x \theta_1(1,t) = 0. \tag{4.5}$$

To solve (4.4) and (4.5) we use separation of variables, writing $\theta_1(x,t) = g(x)f(t)$ and substituting the result into (4.4) to obtain two equations for $g(x)$ and $f(t)$. The function $g(x)$ is determined by the solution of the eigenvalue problem:

$$(1+\xi)\partial_{xx} g + Pg = 0, \qquad \partial_x g(0) = 0, \qquad \partial_x g(1) = 0. \tag{4.6}$$

Here the separation constant $\xi = (P - \pi^2)/\pi^2$ is the relative difference between the applied load P and the dimensionless buckling load, $P_c = \pi^2$ for a purely elastic rod that is simply supported at its ends. The function $f(t)$ satisfies

$$\frac{\xi f(t)}{\delta} = \sum_{n=1}^{\infty} \gamma_n \int_0^t \mathrm{e}^{-\lambda_n (t-t')} \partial_{t'} f(t') \, \mathrm{d}t'. \tag{4.7}$$

Using Laplace transforms ($\mathcal{L}(f(t)) = \int_0^\infty \mathrm{e}^{-st} f(t) \, \mathrm{d}t$), we solve (4.7) and find that

$$f(t) = -\sum_{s \in S} \mathrm{e}^{st} f(0) \sum_{n=1}^{\infty} \frac{\gamma_n}{\lambda_n + s}, \tag{4.8}$$

where $f(0)$ is determined by the initial condition and the set S is composed of elements that satisfy

$$\frac{\xi}{\delta} - \sum_{n=1}^{\infty} \frac{\gamma_n s}{\lambda_n + s} = 0. \tag{4.9}$$

The growth rate at the onset of the dynamic buckling instability is therefore given by the largest s that satisfies (4.9). In figure 4, we plot the growth rate s as a function of the rescaled external load

$$\frac{\xi}{\delta} = \frac{P - P_c}{\delta P_c},$$

with $P_c = \pi^2$, obtained by solving (4.6) and (4.9). When $s < 0$ we do not have an instability, corresponding to the case when $P < P_c$. In the poroelastic regime, when $P_c < P < P_c(1 + \frac{1}{4}\delta)$, fluid flows across the filament in response to the stress gradient in the transverse direction, and the phenomenon is qualitatively different from the buckling of a purely elastic rod. Since the time it takes fluid to flow across the filament is longer than the time it takes a bending wave to propagate the length of the filament, poroelastic buckling is sometimes called creep buckling (Biot 1964).

We now turn to the dependence of the buckling transition on the surface permeability parameter Bi. Substituting a pressure field of the form

$$p(x, r, \phi, t) = h(r) \partial_x \Theta(x) \sin\phi \, \mathrm{e}^{st} \quad \text{and} \quad \theta(x, t) = \mathrm{e}^{st} \Theta(x)$$

into (3.9) yields

$$sh - \frac{1}{r} \partial_r (r \partial_r h) + \frac{h}{r^2} = sr, \tag{4.10}$$

subject to boundary conditions (3.10), which are now given by

$$\left.\begin{aligned} h &= 0 \quad \text{at } r = 0, \\ Bi\, h + \partial_r h &= 0 \quad \text{at } r = 1. \end{aligned}\right\} \tag{4.11}$$

Thus, (4.10) yields $\lim_{s \to 0} h = 0$ and $\lim_{s \to \infty} h = -r$, corresponding to the case of infinitely slow and infinitely fast growth rates respectively. Consequently, for infinitely slow buckling the fluid supports no load. In the case $s \to \infty$ near $r = 1$, a boundary layer emerges where the internal solution ($h = r$) is matched to the boundary condition (4.11) at $r = 1$. Balancing the first two terms of (4.10), the length-scale of the boundary layer $l_{\mathrm{bl}} \sim 1/\sqrt{s}$ or, in dimensional terms,

$$l_{\mathrm{bl}} \sim \sqrt{\frac{(\mu + \lambda)k}{s[(\mu + \lambda)\beta + \alpha^2]}}.$$

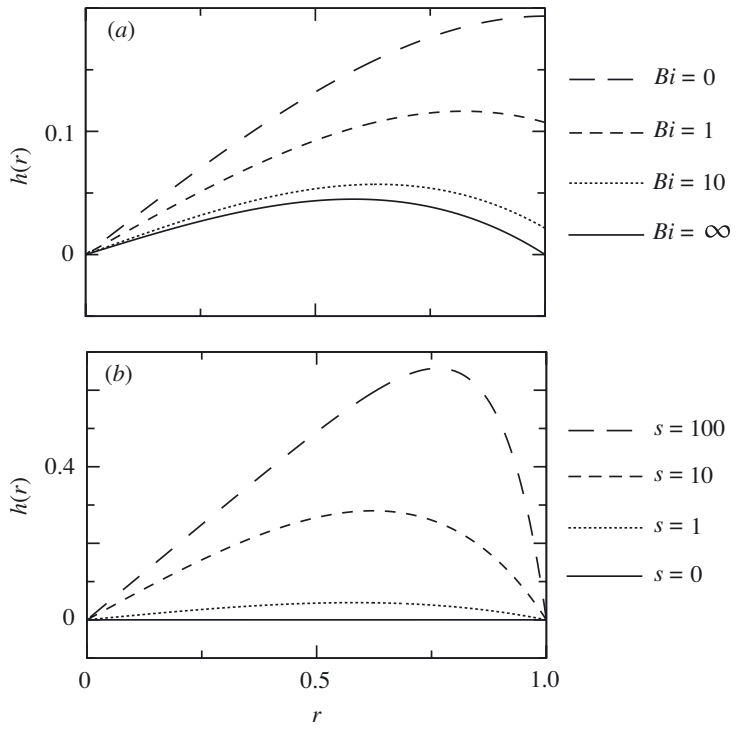

Figure 5. The radial variation of the fluid pressure at the onset of buckling, $h(r)$, for (a) growth rate $s = 1$ and various values of the surface permeability parameter Bi (larger Bi corresponds to a more permeable surface) and (b) $Bi = \infty$ and various s.

To complement these asymptotic results, we solve (4.10) and (4.11) numerically and plot the radial variation in the pressure. In figure 5a we show $h(r)$ for $s = 1$ and various Bi, and in figure 5b we show $h(r)$ for $Bi = \infty$ and various s. As expected, we see that, as the surface permeability increases (i.e. Bi increases) for a given growth rate of the instability (corresponding to a given load), the pressure variations across the filament decrease. On the other hand, as the growth rate increases, a boundary layer appears in the vicinity of the free surface of the rod to accommodate the slow permeation of fluid in response to the stress gradients.

Having considered the onset of poroelastic buckling, we now turn to the transition from poroelastic to inertial dynamics which occurs for very large compressive loads when the fluid cannot move rapidly enough to keep up with the elastic deformations. For large s the condition that determines the growth rate (4.9) reads

$$0 \approx \frac{\xi}{\delta} - \sum_n \gamma_n \left(1 - \frac{\lambda_n}{s}\right). \tag{4.12}$$

We have computed $\sum_n \gamma_n = \frac{1}{4}$ for integrals of Bessel functions. Using the definition of the separation constant $\xi = P/P_c - 1$, we solve equation (4.12) for the growth rate:

$$s \approx \sum_n \gamma_n \lambda_n \left[\frac{P - P_c}{\delta P_c} - \frac{1}{4}\right]^{-1}, \tag{4.13}$$

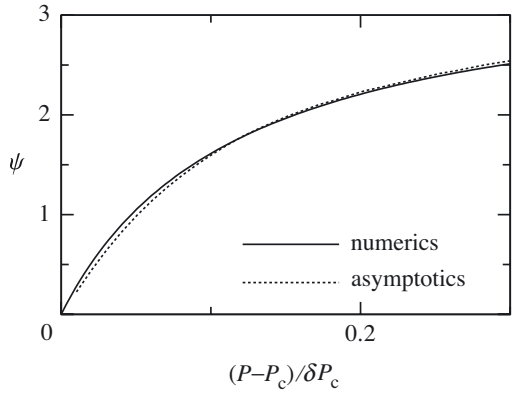

Figure 6. As the solution approaches the equilibrium shape, the difference between the current and equilibrium shape decays exponentially with a rate ψ, which is plotted against the applied compression. $\delta = 1$, $Bi = 0.1$, $\mathrm{d}x = 0.01$, $\mathrm{d}t = 0.01$. The numerical computation is begun with $\theta = 0.9\theta_0$.

showing that it indeed diverges when $(P - P_c)\delta P_c \to \frac{1}{4}$, consistent with figure 4.

(*b*) *Long-time dynamics, $t \gg 1$*

In the long-time limit $t \gg 1$, i.e. when the fluid has enough time to diffuse across and along the filament, the shape of the filament approaches that of the ideal *elastica*. To capture the dynamics of this process, we linearize (3.21) about the steady-state solution by letting

$$\theta = \theta_0(x) + \epsilon\theta_1(x,t) \tag{4.14}$$

with $\epsilon \ll 1$. Substituting the expansion (4.14) into (3.21), at leading order we get

$$\partial_{xx}\theta_0 + P\sin\theta_0 = 0. \tag{4.15}$$

At $O(\epsilon)$, we get

$$\partial_{xx}\theta_1 + P\cos(\theta_0)\theta_1 + \delta\sum_n \gamma_n \int^t \mathrm{e}^{-\lambda_n(t-t')}\partial_{xxt'}\theta_1\,\mathrm{d}t' = 0. \tag{4.16}$$

To simplify the equations further we consider the convolution integral in (4.16) for typical values of $Bi = 0.1$, corresponding to the case for soft gels and biological materials. Then (3.13) yields

$$\{\lambda_n\} = \{3.67, 28.6, 73.1, 137, 221, 325, \dots\} \quad \text{and} \quad \sum_{n=2}^{\infty}\frac{\gamma_n}{\gamma_1} = 0.0152.$$

Given the large separation between the decay constants, we see that the dominant contribution in the integral arises from λ_1, leading to an approximation of (4.16) that reads

$$\partial_{xx}\theta_1 + P\cos(\theta_0)\theta_1 + \delta\gamma_1 \int^t \mathrm{e}^{-\lambda_1(t-t')}\partial_{xxt'}\theta_1\,\mathrm{d}t' = 0. \tag{4.17}$$

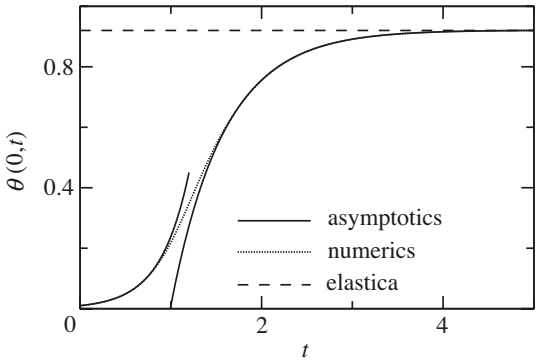

Figure 7. $\theta(0,t)$ for $P = 11$, $\delta = 1$, $Bi = 0.1$, $\mathrm{d}x = 0.01$, $\mathrm{d}t = 0.001$ and $\theta(x,0) = \theta(x,\mathrm{d}t) = 0.01\cos\pi x$. The short-time asymptotic is for a growth rate $s(P)$ found from equation (4.9). The long-time asymptotic is of the form $A\mathrm{e}^{-\psi t} + \theta_0$, where ψ is the rate of decay to the equilibrium angle θ_0 and A is a fitting parameter.

Using separation of variables, $\theta_1(x,t) = g(x)f(t)$, we find that $g(x)$ is given by the solution of the eigenvalue problem

$$(1-\xi)\partial_{xx}g + P\cos(\theta_0)g = 0, \qquad \partial_x g(0) = 0, \qquad \partial_x g(1) = 0, \tag{4.18}$$

while the temporal part $f(t)$ satisfies

$$-f\xi = \delta\gamma_1 \int^t \mathrm{e}^{-\lambda_1(t-t')}\partial_{t'} f \,\mathrm{d}t'. \tag{4.19}$$

Since we are interested in the asymptotic behaviour for $t \gg 1$, we multiply both sides of equation (4.19) by $\mathrm{e}^{\lambda_1 t}$ and differentiate with respect to time to find

$$\partial_t f = \frac{-\lambda_1\xi}{\delta\gamma_1 + \xi} f \equiv -\psi f. \tag{4.20}$$

We observe that the poroelastic solution approaches the elastic steady shape exponentially fast at late times. In figure 6, we plot the exponent $\psi = \lambda_1\xi/(\delta\gamma_1 + \xi)$ versus $(P - P_\mathrm{c})/\delta P_\mathrm{c}$ and see that, the larger the value of P, the faster the solution approaches the final shape.

(*c*) *Intermediate-time dynamics*

For intermediate times we have to solve for the shape of the poroelastica numerically. Our arguments in the previous subsection allow us to neglect the contributions from the higher modes, so that a good approximation to (3.21) is given by

$$\partial_{xx}\theta + P\sin\theta + \gamma_1 \int_0^t \mathrm{e}^{-\lambda_1(t-t')}\partial_{xxt'}\theta \,\mathrm{d}t' = 0. \tag{4.21}$$

For ease of solution, we convert the integro-differential equation to a partial differential equation by multiplying (4.21) by $\mathrm{e}^{\lambda_1 t}$ and differentiating with respect to time, so that

$$(1+\gamma_1)\partial_{xxt}\theta + \lambda_1\partial_{xx}\theta + P\cos\theta\partial_t\theta + \lambda_1 P\sin\theta = 0. \tag{4.22}$$

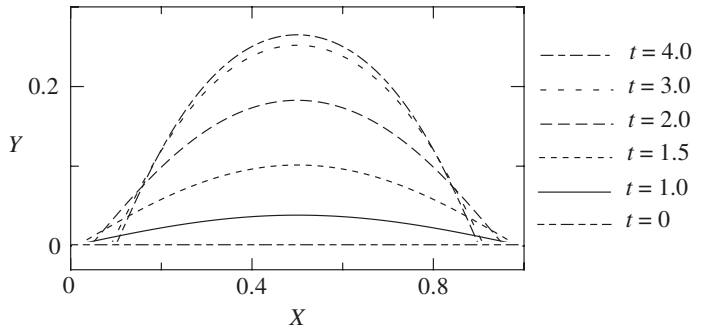

Figure 8. The shape of the buckling filament $X(x,t)$, $Y(x,t)$ for $P = 11$, $\delta = 1$, $Bi = 0.1$, $\mathrm{d}x = 0.01$, $\mathrm{d}t = 0.001$ and $\theta(t=0) = \theta(t=\mathrm{d}t) = 0.01\cos\pi x$.

We solve equation (4.22) subject to the boundary conditions (4.1) using a Crank–Nicolson finite-difference scheme in space and we extrapolate the nonlinearity using the previous two time-steps. This gives us a scheme with second-order accuracy in time. For a time-step $\mathrm{d}x = 0.01$ and a space step $\mathrm{d}t = 0.001$, the difference between the numerical and analytical initial growth rate is 0.2% (see figure 4). In figure 7 we show the variation of the angle $\theta(0,t)$, determined using the numerical simulation for the case when the dimensionless buckling load is slightly larger than the threshold for the poroelastic buckling, with $(P - P_\mathrm{c})/P_\mathrm{c} \sim 0.17$. For comparison, we also show the asymptotic solutions for short and long times determined in the previous sections, and find that they agree well with the numerical solution. To determine the shape of the filament we use the kinematic relations

$$\partial_x X = \cos\theta, \qquad \partial_x Y = \sin\theta, \tag{4.23}$$

where $X(x,t)$ and $Y(x,t)$ are the position of the centreline. Figure 8 shows the shape of the filament as it evolves from the initially unstable straight shape to the final elastic equilibrium via a transient overdamped route. In sharp contrast, a purely elastic rod subjected to the same initial and boundary conditions would vibrate about the final state forever (in the absence of any damping).

5. Displacement-controlled planar buckling

In many problems involving instabilities there is a qualitative difference between load-controlled and displacement experiments. To understand the difference, we consider the problem of displacement-controlled buckling of a poroelastic filament and compare the results with those of the previous section. Since the centreline of the filament is assumed to be inextensible, the change in the end-to-end distance is given by

$$\Delta(t) = 1 - \int_0^1 \cos\theta(x,t)\,\mathrm{d}x. \tag{5.1}$$

We choose the functional form

$$\Delta(t) = \tfrac{1}{2}\Delta_\mathrm{max}[1 + \tanh at], \tag{5.2}$$

to allow us to ramp up the displacement to a maximum amplitude Δ_max at a characteristic rate $\frac{1}{2}\Delta_\mathrm{max}a$. The shape of the poroelastica is now determined by the solution

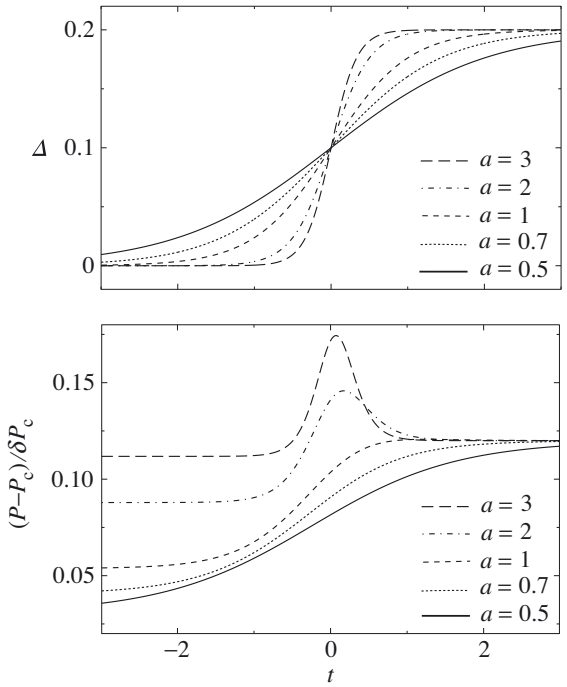

Figure 9. $(P - P_c)/\delta P_c$, where P is the load and P_c is the critical load required for buckling, corresponding to a change in end-to-end displacement $\Delta(t) \approx 0.1[1 + \tanh at]$, for various a. For some later times the more quickly applied displacement, corresponding to larger a, requires a lower compressive force. The graphs correspond to the following parameter values: $\mathrm{d}x = 0.01$, $\mathrm{d}t = 0.002$, $Bi = 0.1$, $\delta = 1$, $\theta(-3) = \theta(-3 + \mathrm{d}t) = 2\sqrt{\Delta(-3)}\cos \pi x$.

of (4.22), (5.1) and (5.2); the unknown load $P(t)$ is now determined at every time-step by using an iteration method to enforce (5.1). For an initial guess to start this procedure, we note that after the onset of buckling when $P > P_c$ for small amplitudes $\theta = \epsilon \cos \pi x$ ($\epsilon \ll 1$) is a solution of (4.22) and (4.1). Substituting into (5.1) gives

$$\Delta = 1 - \int_0^1 \cos(\epsilon \cos \pi x)\, \mathrm{d}x \approx \tfrac{1}{4}\epsilon^2. \tag{5.3}$$

Therefore, we choose $\theta(x, t_0) \sim 2\sqrt{\Delta(t_0)}\cos \pi x$. In figure 9*b*, we show the evolution of the load $P(t)$ for various values of a. P is roughly constant for very short and very long times, but changes as Δ varies quickly for intermediate times. We can understand the initial plateau by considering the case when $\mathrm{e}^{at} \ll 1$, so that (5.2) yields

$$\Delta = \tfrac{1}{2}\Delta_{\max}\left[1 - \frac{1 - \mathrm{e}^{2at}}{1 + \mathrm{e}^{2at}}\right] \approx \Delta_{\max}\mathrm{e}^{2at}. \tag{5.4}$$

In light of the geometrical constraint (5.3) valid for small displacements, this yields

$$\theta \approx 2\sqrt{\Delta_{\max}}\mathrm{e}^{at}\cos \pi x. \tag{5.5}$$

Comparing this with the short-time behaviour of the poroelastic filament considered in § 4 *a*, we see that exponential growth of small angles corresponds to a constant

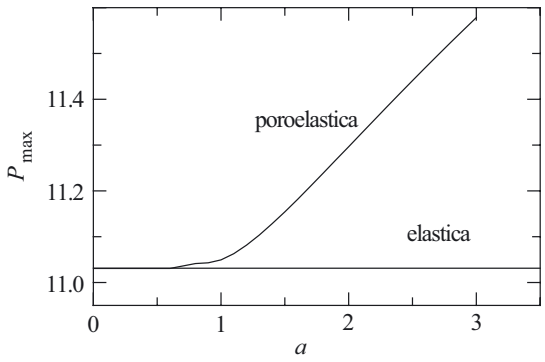

Figure 10. Maximum compressive load, $P_{\max}$, for displacement-controlled buckling, where the displacement field is given by $\Delta(t) \approx 0.1[1 + \tanh at]$. $Bi = 0.1$, $\delta = 1$, $\mathrm{d}t = 0.01$, $\mathrm{d}x = 0.01$.

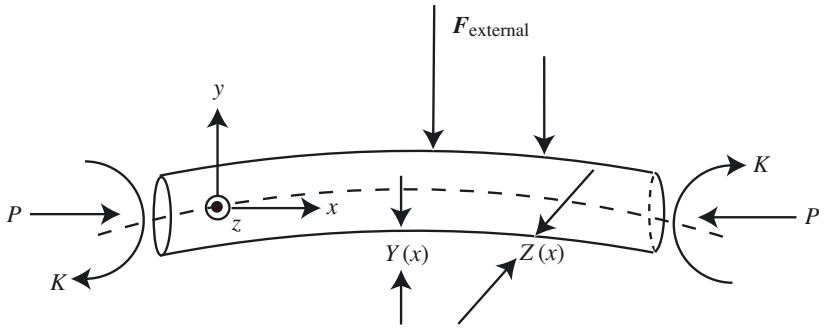

Figure 11. Schematic of a rod buckling under an applied twist and compression in an external medium. $Y(x,t)$ and $Z(x,t)$ are the displacements of the centreline in the y- and z-directions respectively. The dotted line denotes the axis of symmetry.

compressive force seen in figure 9. A similar argument holds for late times, when the system relaxes to its purely elastic equilibrium. For intermediate times, the load can be larger than that for the case of a purely elastic filament. The difference in the loads is due to the fluid resistance in the porelastica. A way of visualizing this is shown in figure 10. For slowly applied displacement fields $P_{\max}$ is almost the same for the elastic and poroelastic cases; however, for rapidly applied displacements, corresponding to large values of a, the compressive force in the poroelastic case is larger due to fluid resistance arising from the pressure gradients across the bending filament.

6. Filament embedded in an external elastic medium and subjected to axial torque and axial thrust

We finally turn to the case of a rod embedded in an external medium subjected to an axial moment, K, and a compressive force P (see figure 11). The presence of the twist causes the instability to become non-planar, and the filament adopts a helical conformation; the presence of an external medium typically causes the instability to manifest itself with a higher wavenumber than would occur otherwise. Letting the displacements of the centreline in the y- and z-directions be $Y(x,t)$, $Z(x,t)$ respectively, we scale the kinematic variables accordingly to define the dimensionless

displacements

$$Y = RY', \qquad Z = RZ'. \tag{6.1}$$

The dimensionless axial moment is defined as

$$K = \frac{\pi(2\mu^2 + 3\lambda\mu)R^4}{4(\mu+\lambda)L}K'.$$

If the transverse displacements of the filament are small, the resistance of the external medium can be approximated well using the response of a linear Hookean solid. In light of the analogy between linear elasticity and Stokes flow, we can use the results of classical slender-body theory in hydrodynamics (Batchelor 1970; Cox 1970) and write the vector of dimensionless external forces on the filament as $\boldsymbol{F}'_{\rm ext} = (0, -\frac{1}{4}\pi EY, -\frac{1}{4}\pi EZ)$, where the dimensionless parameter E is given by

$$E = \frac{16\mu_{\rm m}L^2(\mu+\lambda)}{\ln(L/R)R^2(2\mu^2+3\mu\lambda)}, \tag{6.2}$$

where $\mu_{\rm m}$ is the Lamé coefficient of the surrounding medium. This approximation is valid when $R/L \ll 1$, a condition consistent with the geometry of a thin filament. We will further assume that the filament is free to rotate in the medium, i.e. there is no torque resisting this mode of motion, which varies in any case as R^2 and is thus negligible in most situations.

To derive the evolution equation for the shape of the filament, we use the constitutive equation (2.3) to write down equations for the balance of forces in the y- and z-directions as for the planar filament. After dropping primes this leads to

$$\partial_{xxxx}Y + K\partial_{xxx}Z + \delta\sum_{n=1}^{\infty}\gamma_n\int_0^t \mathrm{e}^{-\lambda_n(t-t')}\partial_{xxxxt}Y\,\mathrm{d}t' + P\partial_{xx}Y + EY = 0, \tag{6.3}$$

$$\partial_{xxxx}Z - K\partial_{xxx}Y + \delta\sum_{n=1}^{\infty}\gamma_n\int_0^t \mathrm{e}^{-\lambda_n(t-t')}\partial_{xxxxt}Z\,\mathrm{d}t' + P\partial_{xx}Z + EZ = 0, \tag{6.4}$$

where, since equation (3.9) is linear, we have superposed the two solutions for bending in the y- and z-directions. Taking $\zeta = Y + \mathrm{i}Z$, equations (6.3) and (6.4) may be written as a single equation for the complex variable ζ:

$$0 = \partial_{xxxx}\zeta - \mathrm{i}K\partial_{xxx}\zeta + P\partial_{xx}\zeta + E\zeta + \delta\sum_{n=1}^{\infty}\gamma_n\int_0^t \mathrm{e}^{-\lambda_n(t-t')}\partial_{xxxxt'}\zeta\,\mathrm{d}t'. \tag{6.5}$$

For a simply supported filament, the corresponding boundary conditions at the ends are

$$\zeta(0) = \zeta(1) = \partial_{xx}\zeta(0) - \mathrm{i}K\partial_x\zeta(0) = \partial_{xx}\zeta(1) - \mathrm{i}K\partial_x\zeta(1) = 0. \tag{6.6}$$

We can treat equations (6.5) and (6.6) in exactly the same fashion as the planar problem and use separation of variables $\zeta(x,t) = g(x)f(t)$ to get

$$\left.\begin{aligned}(1+\xi)\partial_{xxxx}g - \mathrm{i}K\partial_{xxx}g + P\partial_{xx}g + Eg = 0,\\ g(0) = g(1) = \partial_{xx}g(0) - \mathrm{i}K\partial_x g(0) = \partial_{xx}g(1) - \mathrm{i}K\partial_x g(1) = 0,\end{aligned}\right\} \tag{6.7}$$

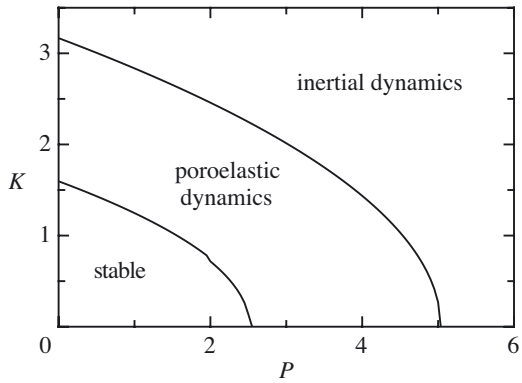

Figure 12. For the case of an applied compression P and axial twisting moment K, we show the three short-time regimes (stable, poroelastic, and inertial) as in figure 4. $E = \delta = 1$.

an eigenvalue problem for the separation constant ξ and $g(x)$. The temporal part of the solution $f(t)$ satisfies

$$\frac{\xi}{\delta} - \sum_{n=1}^{\infty} \frac{\gamma_n s}{\lambda_n + s} = 0, \tag{6.8}$$

which is the same as equation (4.19) for the temporal part of the solution for planar buckling. Thus, once the separation constant ξ is found, equation (4.9) yields the growth rate $s(P, K, E, \delta, Bi)$ as a function of the loading parameters and the material constants (see figure 4).

As an example of how the influence of an external medium can lead to higher modes becoming unstable at lower compressions than the fundamental mode, we consider equation (6.7) in the case $K = 0$,

$$(1 + \xi)\partial_{xxxx}\zeta + P\partial_{xx}\zeta + E\zeta = 0, \tag{6.9}$$

which is an eigenvalue problem for ξ and ζ for a given P. At the ends ($x = 0$ and $x = 1$), the displacements and bending moments vanish, so that the boundary conditions associated with (6.9) are $\zeta(0) = \partial_{xx}\zeta(0) = \zeta(1) = \partial_{xx}\zeta(1) = 0$. The only non-zero solutions to (6.9) occur when $\zeta = \sin q_n x$, where $q_n = n\pi$, $n = 1, 2, \ldots$. The critical compression $P_c(n)$, where the nth mode becomes unstable, is found to be (Landau & Lifshitz 1970)

$$P_c(n) = \pi^2 n^2 + \frac{E}{\pi^2 n^2}. \tag{6.10}$$

We see that the critical buckling load for a given mode number n increases as the stiffness of the environment E increases. Furthermore, for large E, the chosen mode shape does not correspond to the fundamental mode $n = 1$, since $\partial P_c/\partial n = 0$ yields $n = \frac{1}{\pi}E^{1/4}$ for an infinite rod. Physically, this occurs because short-wavelength modes do not deform the stiff elastic environment as much, while the penalty associated with a higher curvature is not too much of a price to pay.

For the case when $K \neq 0$, we cannot solve the eigenvalue problem analytically, and we present the results using the phase diagram shown in figure 12. We find three distinct regimes: for $s < 0$ the system is stable; for $0 < s < \infty$ we have the poroelastic regime where the system buckles on the same time-scale as the fluid pressure diffuses;

Table 2. *Applications of poroelasticity in biology*

application	μ (Pa)	α	k (m^2 Pa^{-1} s^{-1})	R (m)	τ_p (s)
actin cytoskeleton	10^2	0.8	10^{-12}	10^{-6}	10^{-2}
bones	10^{10}	0.05	10^{-14} to 10^{-16}	10^{-2}	10^{-2} to 10^{-3}
cartilage	10^6	0.8	1×10^{-16} to 6×10^{-16}	10^{-3}	10^3
plant stem/root	10^8	0.8	10^{-11}	10^{-2}	10^{-2}
Venus fly trap leaf	10^6	0.8	10^{-12}	10^{-3}	10^{-2}

finally, we have the elastic regime where the system buckles so fast that the fluid does not move and all the deformation occurs in the solid skeleton.

7. Discussion

The usefulness of poroelastic theory is limited to a range of time-scales. The poroelastic time-scale associated with decay of pressure fields is

$$\tau_\mathrm{p} \sim \frac{\alpha^2 R^2}{\mu k},$$

recalling that α is the fluid volume fraction, R is the smallest macroscopic length-scale of the system ($R \gg l_\mathrm{p}$), μ is the effective Lamé coefficient of the composite material, and $k \sim l_\mathrm{p}^2/(\rho\nu)$ is the matrix permeability. If the time-scale of the forcing, $\tau \ll \tau_\mathrm{p}$, the fluid will not move relative to the solid and Hookean elasticity and the effects of inertia are sufficient to describe the system adequately. If $\tau \gg \tau_\mathrm{p}$, the fluid pressure will equilibrate with the surroundings and once again classical elasticity suffices to describe the system, albeit with different Lamé coefficients. However, if $\tau \sim \tau_\mathrm{p}$, the dynamics will be governed by poroelasticity.

Biological systems are composed mainly of fluid—so poroelasticity will be applicable at some time-scale (see table 2 for estimates). Furthermore, they are characterized by extreme geometries (e.g. beams, plates and shells), which led us to consider in detail the dynamics of slender poroelastic objects, and particularly the buckling of a planar filament. Biological materials are usually anisotropic and we expect the permeability and elasticity tensors to reflect this feature. Taking k_l to be the permeability in the axial direction, we can neglect axial diffusion if $(k_l R^2)/(kL^2) \ll 1$. The opposite limit, where $(k_l R^2)/(kL^2) \gg 1$, has been studied by Cederbaum *et al.* (2000). The dynamical behaviour of these objects is separated into two different regimes, one governed by fast inertial effects, and the other by the slow dynamics of fluid flow. These regimes are of course well known in bulk materials (Biot 1956*a*, *b*), but here they appear in a slightly different guise due to the effect of the slender geometry of the system. The onset of planar poroelastic load-controlled buckling was first considered by Biot (1964). In this paper we broaden and deepen our understanding of this phenomenon. An important outcome of our studies is the *poroelastica* equation, which is a simple integro-differential equation with one time constant that describes the dynamics of a poroelastic filament under a compressive load. The bending resistance of the filament is analogous to a (fictional) Maxwell material, where the time constant is the rate at which the pressure field decays (determined by the material parameters and the geometry). We then used this equation to study not

only the onset of buckling, but also the entire dynamics up until saturation for both load-controlled and displacement-controlled buckling.

A series of three-point-bending experiments (Scherer 1992, 1996) has shown that the mechanical response of a silica-gel rod immersed in acetone or ethanol can be described using poroelastic theory. The theory developed by Scherer (1992) applies only to situations where the displacement is applied much faster than the poroelastic time-scale and is a special case of the more general theory presented in this paper. The lack of experiments on slender poroelastic filaments being deformed on the poroelastic time-scale prevents us from testing our predictions quantitatively. Since our results are relevant to swollen polymer networks, gel actuators and sensors, the mechanics of cartilaginous joints, and the physics of rapid movements in plants, an important next step is the quantitative experimental study of slender poroelastic structures.

We acknowledge support via the Norwegian Research Council (J.M.S.), the US Office of Naval Research Young Investigator Program (L.M.), the US National Institutes of Health (L.M.) and the Schlumberger Chair Fund (L.M.). The authors thank Mederic Argentina for insightful discussions.

Appendix A. Derivation of the poroelasticity equations

The derivations of the equations of poroelasticity have been many and varied. This has partly been because several qualitatively different parameter regimes, containing distinct leading-order force balances, exist. We focus here on the equations which govern the second row of table 1, namely where the Stokes length is much larger than the pore size, i.e. $L_\mathrm{s} \gg l_\mathrm{p}$. The methods used to derive equations for this region of parameter space can be classified into three categories: physical arguments and superposition (Biot 1941; Biot & Willis 1957), mixture theory (Barry & Holmes 2001) and microstructural derivations (Auriault & Sanchez-Palencia 1977; Burridge & Keller 1981; Mei & Auriault 1989). First, we show in detail a version of the microstructural derivations, which uses ideas from both Burridge & Keller (1981) and Mei & Auriault (1989).

The equations that govern the behaviour in the incompressible interstitial fluid at low *Re* are

$$\boldsymbol{\sigma}_\mathrm{f} = -p\boldsymbol{I} + 2\epsilon\mu\boldsymbol{e}(v), \tag{A 1}$$

$$\nabla \cdot \boldsymbol{\sigma}_\mathrm{f} = 0, \tag{A 2}$$

$$\nabla \cdot \boldsymbol{v} = 0, \tag{A 3}$$

where σ_f is the stress tensor in the fluid, $\epsilon = l_\mathrm{p}/l_\mathrm{m} \ll 1$ (see figure 13), $\boldsymbol{e}(\cdot) = \frac{1}{2}[\nabla(\cdot) + \nabla(\cdot)^\mathrm{T}]$ is the strain operator, and $\boldsymbol{v}$ is the fluid velocity.

In the solid the analogous equations are

$$\boldsymbol{\sigma}_\mathrm{s} = \boldsymbol{A} : \boldsymbol{e}(u), \tag{A 4}$$

$$\nabla \cdot \boldsymbol{\sigma}_\mathrm{s} = 0, \tag{A 5}$$

where $\boldsymbol{u}$ is the displacement field, $\boldsymbol{A}$ is the tensor of elastic moduli, and σ_s is the stress tensor in the solid. At the solid–fluid interface the continuity of displacements

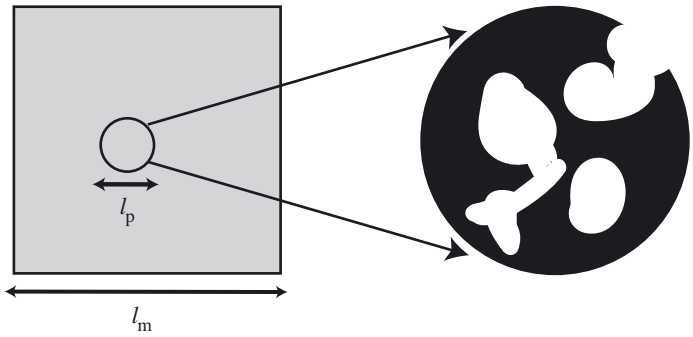

Figure 13. A typical porous medium illustrating the separation of length-scales, where l_p is the pore scale and l_m is the system scale.

and tractions yields

$$\boldsymbol{v} - \partial_t \boldsymbol{u} = 0, \tag{A 6}$$

$$\boldsymbol{\sigma}_\mathrm{s} \cdot \boldsymbol{n} - \boldsymbol{\sigma}_\mathrm{f} \cdot \boldsymbol{n} = 0. \tag{A 7}$$

Here $\boldsymbol{n}$ is the unit normal vector to the surface separating the two phases.

Looking for a perturbation solution in terms of the small parameter ϵ, we use an asymptotic expansion of the variables

$$\left.\begin{aligned} \boldsymbol{\sigma}_\mathrm{f} &= \boldsymbol{\sigma}_\mathrm{f}^0 + \epsilon\boldsymbol{\sigma}_\mathrm{f}^1 + \cdots, \\ \boldsymbol{\sigma}_\mathrm{s} &= \boldsymbol{\sigma}_\mathrm{s}^0 + \epsilon\boldsymbol{\sigma}_\mathrm{s}^1 + \cdots, \\ p &= p^0 + \epsilon p^1 + \cdots, \\ \boldsymbol{u} &= \boldsymbol{u}^0 + \epsilon\boldsymbol{u}^1 + \cdots, \\ \boldsymbol{v} &= \boldsymbol{v}^0 + \epsilon\boldsymbol{v}^1 + \cdots, \end{aligned}\right\} \tag{A 8}$$

with a multiple-scale expansion for the gradient

$$\nabla = \nabla_{x'} + \epsilon\nabla, \tag{A 9}$$

where x denotes the macroscopic scale, $x' = \epsilon x$ denotes the pore scale, ∇ denotes the gradient relative to the macroscopic scale, and $\nabla_{x'}$ denotes the gradient relative to the pore scale. Since we assume that the flow is driven on the macrosopic scale, the leading-order deformation is a function only of x. Then, equations (A1) and (A9) yield the following expressions for the fluid and solid stress tensors:

$$\boldsymbol{\sigma}_\mathrm{s}^0 = \boldsymbol{A} : [\boldsymbol{e}(u^0) + \boldsymbol{e}_{x'}(\boldsymbol{u}^1)], \tag{A 10}$$

$$\boldsymbol{\sigma}_\mathrm{s}^1 = \boldsymbol{A} : [\boldsymbol{e}(u^1) + \boldsymbol{e}_{x'}(\boldsymbol{u}^2)], \tag{A 11}$$

$$\boldsymbol{\sigma}_\mathrm{f}^0 = -p^0\boldsymbol{I}, \tag{A 12}$$

$$\boldsymbol{\sigma}_\mathrm{f}^1 = -p^1\boldsymbol{I} + \mu\boldsymbol{e}_{x'}(\boldsymbol{v}^0), \tag{A 13}$$

where $\boldsymbol{e}$ and $\boldsymbol{e}_{x'}$ denote the strain relative to the system-scale and pore-scale coordinates respectively. The stress balance in the fluid (A 5) yields

$$\nabla_{x'} p^0 = 0, \tag{A 14}$$

$$\mu\nabla^2\boldsymbol{v}^0 - \nabla_{x'} p^1 - \nabla p^0 = 0. \tag{A 15}$$

Thus the leading-order pressure gradient $p^0(\boldsymbol{x})$ is only a function of the system scale coordinate. The stress balance in the solid yields

$$\nabla_{x'} \cdot \boldsymbol{\sigma}_{\mathrm{s}}^0 = 0, \tag{A 16}$$

$$\nabla_{x'} \cdot \boldsymbol{\sigma}_{\mathrm{s}}^1 + \nabla \cdot \boldsymbol{\sigma}_{\mathrm{s}}^0 = 0. \tag{A 17}$$

We define $\boldsymbol{\sigma}$ to be the total stress tensor:

$$\boldsymbol{\sigma} = \begin{cases} \boldsymbol{\sigma}_{\mathrm{s}} & \text{in } V_{\mathrm{s}}, \\ \boldsymbol{\sigma}_{\mathrm{f}} & \text{in } V_{\mathrm{f}}, \end{cases} \tag{A 18}$$

where V_{s} and V_{f} are the solid and fluid parts of a volume element. Stress balance in the fluid and solid implies

$$\nabla_{x'} \cdot \boldsymbol{\sigma}^1 + \nabla \cdot \boldsymbol{\sigma}^0 = 0. \tag{A 19}$$

Averaging (A19) over the pore scale yields

$$\frac{1}{V}\int \nabla \cdot \boldsymbol{\sigma}^0 \,\mathrm{d}V + \frac{1}{V}\int \nabla_{x'} \cdot \boldsymbol{\sigma}^1 \,\mathrm{d}V = \frac{1}{V}\int \nabla \cdot \boldsymbol{\sigma}^0 \,\mathrm{d}V + \frac{1}{V}\int \boldsymbol{n} \cdot \boldsymbol{\sigma}^1 \,\mathrm{d}S = 0, \tag{A 20}$$

where $V = V_{\mathrm{f}} + V_{\mathrm{s}}$. In the limit $V \to \infty$,

$$\frac{1}{V}\int \boldsymbol{n} \cdot \boldsymbol{\sigma}^1 \,\mathrm{d}S \to 0,$$

since the surface to volume ratio tends to zero. Consequently,

$$\frac{1}{V}\int \nabla \cdot \boldsymbol{\sigma}^0 \,\mathrm{d}V = \nabla \cdot \langle \boldsymbol{\sigma}^0 \rangle = 0, \tag{A 21}$$

$$\langle \boldsymbol{\sigma}^0 \rangle = \langle \boldsymbol{A} : [\boldsymbol{e}(u^0) + \boldsymbol{e}_{x'}(\boldsymbol{u}^1)] \rangle - \phi_{\mathrm{f}} p^0 \boldsymbol{I}, \tag{A 22}$$

where ϕ_{f} is the fluid volume fraction and $\langle \cdot \rangle$ denotes the average over the pore scale. In order to write averaged equations in terms of $\boldsymbol{u}^0$ and p^0, we eliminate $\boldsymbol{u}^1$. This is achieved by using the stress balance in the solid so that

$$\nabla_{x'} \cdot \boldsymbol{\sigma}_{\mathrm{s}}^0 = \nabla_{x'} \cdot \{ \boldsymbol{A} : [\boldsymbol{e}(\boldsymbol{u}^0) + \boldsymbol{e}_{x'}(\boldsymbol{u}^1)] \} = 0. \tag{A 23}$$

The boundary condition (A 7) at the fluid solid surface yields

$$\boldsymbol{A} : [\boldsymbol{e}(u^0) + \boldsymbol{e}_{x'}(\boldsymbol{u}^1)] \cdot \boldsymbol{n} = -p^0 \boldsymbol{n}. \tag{A 24}$$

Since this is a linear system of equations, $\boldsymbol{u}^1$ is a linear combination of p^0 and $\boldsymbol{e}(u^0)$:

$$\boldsymbol{u}^1 = \boldsymbol{B} : \boldsymbol{e}(u^0) - \boldsymbol{C} p^0, \tag{A 25}$$

where the third-rank tensor $\boldsymbol{B}$ and vector $\boldsymbol{C}$ vary on the pore and system scales, and can only be found explicitly by solving the microstructural problem (A 23), (A 24). The averaged stress tensor becomes

$$\langle \boldsymbol{\sigma}^0 \rangle = \langle \boldsymbol{A} + \boldsymbol{A} : \boldsymbol{e}_{x'}(\boldsymbol{B}) \rangle : \boldsymbol{e}(u^0) - \langle \boldsymbol{A} : \boldsymbol{e}_{x'}(\boldsymbol{C}) \rangle p^0 - \phi_{\mathrm{f}} p^0 \boldsymbol{I}, \tag{A 26}$$

where, in index notation, $\boldsymbol{e}_{x'}(\boldsymbol{B}) = (\partial_{x'_{\mathrm{m}}} B_{nkl} + \partial_{x'_n} B_{mkl})$. If we assume that the material is isotropic on the macroscopic scale, we can further reduce (A 26) to

$$\langle \boldsymbol{\sigma}^0 \rangle = 2\mu \boldsymbol{e}(u^0) + \lambda \nabla \cdot \boldsymbol{u}^0 \boldsymbol{I} + (-\phi_{\mathrm{f}} + \gamma) p^0 \boldsymbol{I}, \tag{A 27}$$

where $\gamma \boldsymbol{I} = \langle \boldsymbol{A} : e(\boldsymbol{C}) \rangle$ is an isotropic pressure in the solid due to the fluid pressure exerted at the interface. Substituting (A27) into the stress-balance equation

$$\nabla \cdot \langle \boldsymbol{\sigma}^0 \rangle = 0 \tag{A 28}$$

gives us three equations for the four unknowns ($\boldsymbol{u}^0$ and p^0). We now turn to continuity to give us the final equation. Since the fluid stress balance (A 15) is linearly forced by the external pressure gradient, we can define a tensor $\boldsymbol{k}$ relating the external pressure gradient to the pore-scale flow:

$$\boldsymbol{v}^0 - \partial_t \boldsymbol{u}^0 = -\boldsymbol{k} \cdot \nabla p^0. \tag{A 29}$$

Averaging over the fluid volume yields

$$\langle \boldsymbol{v}^0 \rangle - \phi_{\mathrm{f}} \partial_t \boldsymbol{u}^0 = -\langle \boldsymbol{k} \rangle \cdot \nabla p^0. \tag{A 30}$$

Since the fluid is incompressible, averaging the continuity equation

$$\nabla \cdot \boldsymbol{v}^0 + \nabla_{x'} \cdot \boldsymbol{v}^1 = 0 \tag{A 31}$$

gives

$$\begin{aligned} 0 &= \nabla \cdot \langle \boldsymbol{v}^0 \rangle + \frac{1}{V} \int \nabla_{x'} \cdot \boldsymbol{v}^1 \, \mathrm{d}V = \nabla \cdot \langle \boldsymbol{v}^0 \rangle + \frac{1}{V} \int \boldsymbol{n} \cdot \boldsymbol{v}^1 \, \mathrm{d}S \\ &= \nabla \cdot \langle \boldsymbol{v}^0 \rangle + \frac{1}{V} \int \boldsymbol{n} \cdot \partial_t \boldsymbol{u}^1 \, \mathrm{d}S = \nabla \cdot \langle \boldsymbol{v}^0 \rangle - \frac{1}{V} \int \nabla \cdot \partial_t \boldsymbol{u}^1 \, \mathrm{d}V, \end{aligned} \tag{A 32}$$

where we have used (A 6). Taking the divergence of (A 29) and using (A 32) and (A 25) to eliminate $\boldsymbol{v}^0$ and $\boldsymbol{u}^1$ respectively yields

$$\begin{aligned} -\nabla \cdot \langle \boldsymbol{k} \rangle \cdot \nabla p^0 &= \nabla \cdot (\langle \boldsymbol{v}^0 \rangle - \phi_{\mathrm{f}} \partial_t \boldsymbol{u}^0) \\ &= \langle \nabla_{x'} \cdot \boldsymbol{B} \rangle : \boldsymbol{e}(\partial_t \boldsymbol{u}^0) - \langle \nabla_{x'} \cdot \boldsymbol{C} \rangle \partial_t p^0 - \partial_t \boldsymbol{u}^0 \cdot \nabla \phi_{\mathrm{f}} - \phi_{\mathrm{f}} \nabla \cdot \partial_t \boldsymbol{u}^0. \end{aligned} \tag{A 33}$$

If the change in solid volume fraction is much smaller than the volume fraction itself, $\partial_t \boldsymbol{u}^0 \cdot \nabla \phi_{\mathrm{f}} \approx 0$. Furthermore, if the solid skeleton is incompressible, then $\nabla \cdot \langle \boldsymbol{v}^0 \rangle = 0$, so that the first two terms on the right-hand side of equation (A 33) are negligible. For a compressible isotropic skeleton, (A 33) yields

$$\beta \partial_t p^0 - \nabla \cdot \langle \boldsymbol{k} \rangle \cdot \nabla p^0 = -\alpha \partial_t \nabla \cdot \boldsymbol{u}^0, \tag{A 34}$$

where $\beta = \langle \nabla_{x'} \cdot \boldsymbol{C} \rangle$ is the bulk compliance of the solid skeleton and $\alpha = \phi_{\mathrm{f}} - \frac{1}{3} \langle \nabla_{x'} \cdot \boldsymbol{B} \rangle_{ii}$ is the effective fluid volume fraction. In general if the solid is treated as compressible, the fluid must also be treated as such, since their bulk moduli are comparable. Thus, β is really a measure of the compressibility when the system is jacketed, so that for a mixture of an incompressible solid and fluid, $\beta = 0$. Multiple scale analysis (Auriault & Sanchez-Palencia 1977) shows that $\langle \nabla_{x'} \cdot \boldsymbol{B} \rangle = \langle \boldsymbol{A} : \boldsymbol{e}(\boldsymbol{C}) \rangle = \gamma$, so that (A 27) takes the form

$$\langle \boldsymbol{\sigma}^0 \rangle = 2\mu \boldsymbol{e}(\boldsymbol{u}^0) + \lambda \nabla \cdot \boldsymbol{u}^0 \boldsymbol{I} - \alpha p^0 \boldsymbol{I}. \tag{A 35}$$

Equations (A 28), (A 34) and (A 35) are the equations of poroelasticity, identical in form to the equations written down by Biot (1941). Removing the brackets and superscripts, we recover equations (2.3) and (2.5) from § 2. Studying poroelasticity from the microstructural point of view allows us to see that Biot's (1941) equations correspond to a locally compressible solid skeleton and the equations of mixture theory (Barry & Holmes 2001) correspond to an incompressible solid skeleton.

Appendix B. Equations of motion for a poroelastic sheet

The equations of motion for a sheet of thickness H and length L are found using the same techniques as for a filament. The displacement field $\boldsymbol{u} = (u(y), v(y), 0)$ is two dimensional, where the y-direction is normal to the neutral surface and the free surfaces are located at $y = \pm\frac{1}{2}H$. We use the following dimensionless parameters:

$$\left.\begin{aligned} t = (\beta + \frac{\alpha^2}{2\mu+\lambda})\frac{H^2}{k}t', \qquad p = \frac{2\mu\alpha}{[\beta(2\mu+\lambda)+\alpha^2]}\frac{H^2}{L^2}p', \\ y = Hy', \qquad \sigma_{xx} = \frac{4\mu(\mu+\lambda)}{2\mu+\lambda}\frac{H^2}{L^2}\sigma'_{xx}, \qquad P = \frac{\mu(\mu+\lambda)H^3}{3(2\mu+\lambda)L^2}P'. \end{aligned}\right\} \tag{B 1}$$

The dimensionless parameter δ characterizing the ratio of the fluid stress to the solid stress is

$$\delta = \frac{12\mu\alpha^2}{(\mu+\lambda)[\beta(2\mu+\lambda)+\alpha^2]}. \tag{B 2}$$

The pressure field is found by solving the one-dimensional diffusion equation

$$\partial_t p - \partial_{yy} p = -y\partial_{xt}\theta, \tag{B 3}$$

with the boundary conditions

$$\left.\begin{aligned} \partial_y p + Bi\, p = 0 \quad \text{at } y = \tfrac{1}{2}, \\ -\partial_y p + Bi\, p = 0 \quad \text{at } y = -\tfrac{1}{2}. \end{aligned}\right\} \tag{B 4}$$

Then

$$p = -\sum_n \chi_n \sin\lambda_n y \int_0^t \mathrm{e}^{-\lambda_n(t-t')}\partial_{xt'}\theta \,\mathrm{d}t', \tag{B 5}$$

where the λ_n satisfy

$$\lambda_n \cos\tfrac{1}{2}\lambda_n + Bi \sin\tfrac{1}{2}\lambda_n = 0, \tag{B 6}$$

and χ_n and γ_n are given by

$$\left.\begin{aligned} \chi_n = 2(2+Bi)\sin\tfrac{1}{2}\lambda_n \left(\lambda_n^2\left(1 - \frac{\sin\lambda_n}{\lambda_n}\right)\right)^{-1}, \\ \gamma_n = 2(2+Bi)^2\sin^2\tfrac{1}{2}\lambda_n \left(\lambda_n^4\left(1 - \frac{\sin\lambda_n}{\lambda_n}\right)\right)^{-1}. \end{aligned}\right\} \tag{B 7}$$

(B6) and (B7) together with equation (3.21) describe the motion of a poroelastic plate with time-dependent plane stress.

Appendix C. Kirchhoff–Love theory for a bent, twisted filament

Here we construct the equilibrium equations for a thin poroelastic rod whose deformation is not necessarily in the plane. The case of a purely elastic filament is treated in Love (1944). The configuration is given by the position of the centreline and the orientation of its cross-section at every point along it. At every point along the centreline of the rod $\boldsymbol{r}(\boldsymbol{X}, \boldsymbol{t}) = (X(x,t), Y(x,t), Z(x,t))$, where x is the arc length,

we consider the orthogonal triad $\boldsymbol{d}_i(x,t)$, $i=1,2,3$, where $\boldsymbol{d}_1$ and $\boldsymbol{d}_2$ lie along the principal axes of the cross-section of the rod and

$$\boldsymbol{d}_3 = \partial_x \boldsymbol{r} \tag{C 1}$$

is the vector tangent to the centreline. The orientation is determined by a body-fixed director frame that allows us to consider finite deformations. In this case we use the director basis to follow the evolution of the fluid pressure field. The vector of strains $\boldsymbol{\kappa}$ is given by

$$\boldsymbol{\kappa} = \kappa^{(1)}\boldsymbol{d}_1 + \kappa^{(2)}\boldsymbol{d}_2 + \Omega \boldsymbol{d}_3, \tag{C 2}$$

which defines the rotation of the principal axes along the filament. Here $\kappa^{(1)}$ and $\kappa^{(2)}$ are the projections of the curvature of the centreline onto the principal axes of the cross-section and Ω is the twist strain,

$$\partial_x \boldsymbol{d}_i = \boldsymbol{\kappa} \times \boldsymbol{d}_i. \tag{C 3}$$

The stress resultant vector $\boldsymbol{F}(x,t)$ and the couple resultant vector $\boldsymbol{M}(x,t)$ at any cross-section can be written as

$$\boldsymbol{F} = \sum_{i=1}^{3} F^{(i)}(x,t)\boldsymbol{d}_i(x,t), \qquad \boldsymbol{M} = \sum_{i=1}^{3} M^{(i)}(x,t)\boldsymbol{d}_i(x,t), \tag{C 4}$$

where $F^{(1)}$ and $F^{(2)}$ are the shear forces and $M^{(1)}$ and $M^{(2)}$ are the bending moments along the principal axes, $F^{(3)}$ is the tensile force and $M^{(3)}$ is the twisting moment.

Since the equation for the diffusion of pressure is linear, we consider the bending about the principal axes separately. In light of equation (3.20) ($\partial_x \theta$ being the curvature along one of the principal axes), we can write the equations for the dimensionless couple resultant vector $\boldsymbol{M}$ as

$$\left.\begin{aligned} M^{(1)} &= \kappa^{(1)} + \delta \sum_{n=1}^{\infty} \gamma_n \int_0^t \mathrm{e}^{-\lambda_n (t-t')} \partial_{t'} \kappa^{(1)} \,\mathrm{d}t', \\ M^{(2)} &= \kappa^{(2)} + \delta \sum_{n=1}^{\infty} \gamma_n \int_0^t \mathrm{e}^{-\lambda_n (t-t')} \partial_{t'} \kappa^{(2)} \,\mathrm{d}t', \\ M^{(3)} &= C\Omega, \end{aligned}\right\} \tag{C 5}$$

where $C(=2(\lambda+\mu)(3\lambda+2\mu)^{-1}$ for a circular rod) is the dimensionless torsional rigidity (normalized by the bending contribution to $M^{(1)}$), τ_a is the dimensionless twist strain, and the λ_n are determined by solving equation (3.13). We note that the twisting moment has no poroelastic contribution because it is purely a shear deformation, and poroelastic effects arise only from volumetric deformations, as seen in equation (2.5). Finally, the local balance of forces and torques gives the equilibrium equations

$$\partial_x \boldsymbol{F} + \boldsymbol{F}_{\mathrm{ext}} = 0, \tag{C 6}$$

$$\partial_x \boldsymbol{M} + \boldsymbol{d}_3 \times \boldsymbol{F} = 0, \tag{C 7}$$

where $\boldsymbol{F}_{\mathrm{ext}}$ is the external body force acting on the cross-section. The complete set of equations that determine the poroelastic behaviour of a filament is (C 1) and (C 5)–(C 7).

References

Auriault, J.-L. & Sanchez-Palencia, E. 1977 Étude du comportment macroscopique d'un milieu poreux saturé déformable. *J. Méc.* **16**, 575–603.

Barry, S. I. & Holmes, M. 2001 Asymptotic behaviors of thin poroelastic layers. *IMA J. Appl. Math.* **66**, 175–194.

Batchelor, G. K. 1970 Slender-body theory for particles of arbitrary cross-section in Stokes flow. *J. Fluid Mech.* **44**, 419–440.

Biot, M. A. 1941 General theory of three-dimensional consolidation. *J. Appl. Phys.* **12**, 155–165.

Biot, M. A. 1956*a* Theory of propagation of elastic waves in a fluid-saturated porous solid. I: low frequency range. *J. Acoust. Soc. Am.* **28**, 168–178.

Biot, M. A., 1956*b* Theory of propagation of elastic waves in a fluid-saturated porous solid. II: higher frequency range. *J. Acoust. Soc. Am.* **28**, 179–191.

Biot, M. A. 1964 Theory of buckling of a porous slab and its thermoelastic analogy. *J. Appl. Mech.* **31**, 194–198.

Biot, M. A. & Willis, D. G. 1957 The elastic coefficients of the theory of consolidation. *J. Appl. Mech.* **24**, 594–601.

Bird, R., Armstrong, R. & Hassager, O. 1987 *Dynamics of polymeric fluids*, vol. 1. Wiley.

Burridge, R. & Keller, J. B. 1981 Poroelasticity equations derived from microstructure. *J. Acoust. Soc. Am.* **70**, 1140–1146.

Cederbaum, G., Li, L. P. & Schulgasser, K. 2000 *Poroelastic structures*. Elsevier.

Cox, R. G. 1970 The motion of long slender bodies in a viscous fluid. Part I. General theory. *J. Fluid Mech.* **44**, 791–810.

Landau, L. D. & Lifshitz, E. M. 1970 *Theory of elasticity*, 2nd edn. Oxford: Pergamon.

Love, A. E. H. 1944 *A treatise on the mathematical theory of elasticity*, 4th edn. New York: Dover.

Lydzba, D. & Shao, J. F. 2000 Study of poroelasticity material coefficients as response of microstructure. *Mech. Cohes. Frict. Mater.* **5**, 149–171.

Mei, C. C. & Auriault, J.-L. 1989 Mechanics of heterogeneous porous media with several spatial scales. *Proc. R. Soc. Lond.* A **426**, 391–423.

Scherer, G. W. 1992 Bending of gel beams: method for characterizing elastic properties and permeability. *J. Non-cryst. Solids* **142**, 18–35.

Scherer, G. W. 1996 Influence of viscoelasticity and permeability on the stress response of silica gel. *Langmuir* **12**, 1109–1116.

Selvadurai, A. P. S. (ed.) 1996 *Mechanics of poroelastic media*. Solid Mechanics and its Application, vol. 35. Kluwer.

Wang, H. F. 2000 *Theory of linear poroelasticity with applications to geomechanics and hydrogeology*. Princeton University Press.